

Interplay between domain walls and magnetization curling induced by chemical modulations in cylindrical nanowires

L. Álvaro-Gómez,^{*,†,‡,¶} A. Masseboeuf,[†] N. Mille,[§] C. Fernández-González,^{||} S. Ruiz-Gómez,[⊥]
J.C. Toussaint,[#] R. Belkhou,[§] M. Foerster,^{||} E. Pereiro,^{||} L. Aballe,^{||} C. Thirion,[#]
D. Gusakova,[†] O. Fruchart,[†] and L. Pérez^{‡,¶}

[†]Univ. Grenoble Alpes, CNRS, CEA, Grenoble INP, SPINTEC, 38000 Grenoble, France.

[‡]IMDEA Nanociencia, Campus de Cantoblanco, 28049 Madrid, Spain.

[¶]Dpto. de Física de Materiales, Universidad Complutense de Madrid, 28040 Madrid, Spain.

[§]Synchrotron SOLEIL, l'Orme des Merisiers, Saint-Aubin, FR-91192 Gif-sur-Yvette Cedex, France.

^{||}Alba Synchrotron Light Facility, CELLS, 08290 Cerdanyola del Vallès, Barcelona, Spain.

[⊥]Max Planck Institute for Chemical Physics of Solids, 01187 Dresden, Germany.

[#]Univ. Grenoble Alpes, CNRS, Institut Néel, 38000 Grenoble, France.

Received May 2, 2024; E-mail: laura.alvaro@ucm.es

Abstract: Cylindrical magnetic nanowires have been proposed as a means of storing and processing information in a 3D medium, based on the motion of domain walls (DWs). Introducing short chemical modulations in such wires would allow for reliable digital control of DWs. Here, we outline the intricate physics of the interaction of domain walls with modulations to control their motion, combining micromagnetic simulations and experimental evidence. This interaction combines a long-range moderate magnetostatic repulsion with a local energy well. The latter depends on the respective circulation sense of magnetization in the domain wall and modulation. We also show that a modulation has the ability to switch the internal circulation of a DW upon its propagation, thereby acting as a polarizing component and opening the possibility to exploit not only the position of walls, but also their internal structure.

Cylindrical nanowires made of a soft-magnetic material are a textbook case for investigating magnetization dynamics in a three-dimensional geometry. Their magnetic textures are determined by the nanowire's geometrical and compositional features, as well as by their magnetic history. While the uniaxial shape anisotropy favors an axial magnetization state, magnetic charges occurring at the wire terminations can induce end domains. Theory predicts that when the diameter is larger than circa seven times the dipolar exchange length, $\Delta_d = \sqrt{\frac{2A}{\mu_0 M_s^2}}$, the magnetization rotates around the wire axis in the end domains, which is commonly referred to as curling or vortex state.¹⁻⁴ This configuration decreases magnetostatic energy at the expense of exchange energy, by converting part of the surface charges into volume charges. It is worth noting that extended curling domains may also arise in nanowires with magnetocrystalline anisotropy promoting azimuthal magnetization, as observed in CoNi alloys,⁵ single-crystalline hcp Co⁶⁻⁸ or single-crystal CVD Ni wires.⁹ However, we do not cover this specific case in the present manuscript.

There have been several experimental proofs of end curling: a decrease in remanence with increasing diameter,¹⁰ more rounded hysteresis loops measured with the Kerr effect than with global magnetometry,¹¹ quantitative analysis using magnetic force microscopy,¹² or direct imaging with photo-emission electron microscopy.¹³ Curling also oc-

curs in other situations where axial magnetization gives rise to magnetic charges. One such scenario involves diameter modulation, as observed for nanowires made of FeCoCu,¹⁴ single-crystal Ni,¹⁵ NiFe alloys,^{16,17} or Ni.^{18,19} Another case is the axial modulation of material, resulting in a mismatch of magnetization, such as in Fe₂₀Ni₈₀/Fe₈₀Ni₂₀,^{20,21} Ni/Co,²²⁻²⁴ or Co/Cu.²⁵ The existence of curling textures is particularly relevant with the emergence of spintronic investigations of nanowires.^{21,26-32} Indeed, the axial charge current gives rise to an Oersted field, which directly couples to curling textures and may assist nucleation³³ or switch the sign of curling.²¹

Magnetic domain walls in cylindrical nanowires can manifest as one of two types: a Transverse-Vortex Wall (TVW) or a Bloch-Point Wall (BPW).^{4,34} The characteristic feature of the TVW is a transversal magnetization component with respect to the wire axis, which implies the existence of two areas on the outer surface of the wire where $\mathbf{m} \cdot \mathbf{n} = \pm 1$, where \mathbf{n} is the unit vector normal to the surface. At these locations, the tangential magnetization takes the form of a vortex-antivortex pair.³⁵ The BPW is characterized by a curling magnetization around the wire axis and a magnetic singularity at its core, known as the Bloch point.³⁶⁻³⁸ A feature that clearly distinguishes its topology from that of the TVW is the absence of any point on the wire surface with $\mathbf{m} \cdot \mathbf{n} = \pm 1$, although a radial magnetization component may arise to reduce magnetostatic effects related to the head-to-head or tail-to-tail domains.

The first experimental evidence of a BPW and a TVW in cylindrical nanowires was provided by shadow XMCD-PEEM microscopy in 2014.³⁹ Subsequent studies include investigations of the possible transformation of the wall type under axial magnetic fields⁴⁰ or under current pulses, where it was demonstrated BPW velocities in excess of 600 m · s⁻¹ and the switching of BPW curling with the Oersted field.^{27,29}

Therefore, both chemical modulations and BPWs involve curling of magnetization around the wire axis, and in both cases the sign (circulation sense) can be switched with an anti-parallel Oersted field.^{21,27,29} The similarity of their features naturally raises the question of how these two objects interact with each other. This question is particularly relevant since chemical modulations have been proposed as engineered sites to control domain walls in nanowires. In this manuscript, we examine this interaction, both experimentally and with micromagnetic simulations at rest and under

the stimulus of an applied axial magnetic field. We shed light on the roles of exchange and dipolar energy, in order to understand the different mechanisms involved in domain wall pinning and propagation through a chemical modulation. A special focus is given to the significance of the respective circulations of the wall and modulation, which can either be parallel ($C + C+$) or antiparallel ($C + C-$).

Energy landscape of a DW at a modulation

Micromagnetic simulations

In the following, we describe the energetics of a domain wall in a nanowire. Due to the mostly one-dimensional nature of nanowires, their energy landscape may be reduced to one dimension as in the Becker-Kondorski description.⁴¹ For nanowires with homogeneous composition, ideally, the domain wall energy does not depend on its position, as long as it is far enough from the wire ends. However, in practice, domain walls may be pinned at specific locations, such as material defects or grain boundaries.^{42–44} The introduction of chemical modulations aims to modify the domain wall energy landscape, allowing controlled pinning sites to be established if the artificial pinning strength exceeds that related to material defects. In micromagnetic simulations, one method to extract the energy landscape is to monitor the domain wall energy during its slow drift free of external forces under large damping so that it remains under quasistatic conditions at all times. This approach was successfully used for a diameter-modulated nanowire.⁴⁵ However, in the present case, such a method cannot be easily applied, as the profile of the energy landscape may be non-monotonous so that the drift does not cover all positions. Instead, we applied an axial external magnetic field to move the domain wall towards the chemical modulation. The damping coefficient was set to $\alpha = 1$ to be as close to equilibrium as possible and in a quasi-static situation. Both methods are expected to coincide as long as the applied field does not significantly affect the internal structure of the domain wall, such as its width.

We consider a $d = 90$ nm diameter Permalloy ($\text{Fe}_{20}\text{Ni}_{80}$) nanowire with a $\ell = 20$ nm-long $\text{Fe}_{80}\text{Ni}_{20}$ chemical modulation at $z_{\text{DW}} = 0$, in two situations: parallel and anti-parallel curling circulations of BPW and modulation, $C + C+$ and $C + C-$ respectively. The domain wall is pushed towards the modulation under the application of an external magnetic field oriented along \hat{z} or $-\hat{z}$ for $z_{\text{DW}} < 0$ or $z_{\text{DW}} > 0$, respectively, with magnitude increasing in small steps. The initial circulation of the BPW is chosen with the same sign as the direction of motion, so that it is the stable one during dynamics and thus does not switch spontaneously during motion.⁴⁶ The internal energy, *i.e.*, the sum of the dipolar and exchange energy: $E_0 = E_d + E_{\text{ex}}$, is displayed versus BPW position (z_{DW}) on Figure 1a. z_{DW} is computed as the intercept of the three iso-surfaces of the magnetization field: $m_x = 0$, $m_y = 0$ and $m_z = 0$.⁴⁷ Figure 1b and Figure 1c show outer views of the micromagnetic simulation at selected time steps. At a long distance from the modulation, typically 250 nm or more, both curves overlap and reveal a repulsive interaction. To the contrary, at shorter distances, the respective circulations matter: the repulsion keeps increasing for opposite circulations, giving rise to an energy barrier, while the modulation acts as a local potential well for identical circulations. This can be understood as follows.

(i) At long distances between the BPW and the modulation the interaction is independent of their relative circulations. This is consistent with the known fact that circulations of curling structures do not interact with one another via dipolar interactions,⁴⁸ as the magnetic potential does not depend on the sign of circulation. The repulsion results from the interaction of the positively-charged head-to-head BPW with the dipolar field of the modulation, whose positively-charged interface is the one closest to the wall.²¹ The same repulsion would apply for a negatively charged tail-to-tail BPW, giving rise to a neighboring negatively-charged modulation interface. (ii) At short distances, the magnetization textures of the BPW and the modulation overlap and interact directly via exchange: magnetization gradients decrease for parallel circulation, while they increase for antiparallel circulations (see Figure 1b), which translates into a decrease (resp. increase) of exchange energy. This, again, is consistent with previous reports on the interaction of curling end structures in short nanotubes.⁴⁸

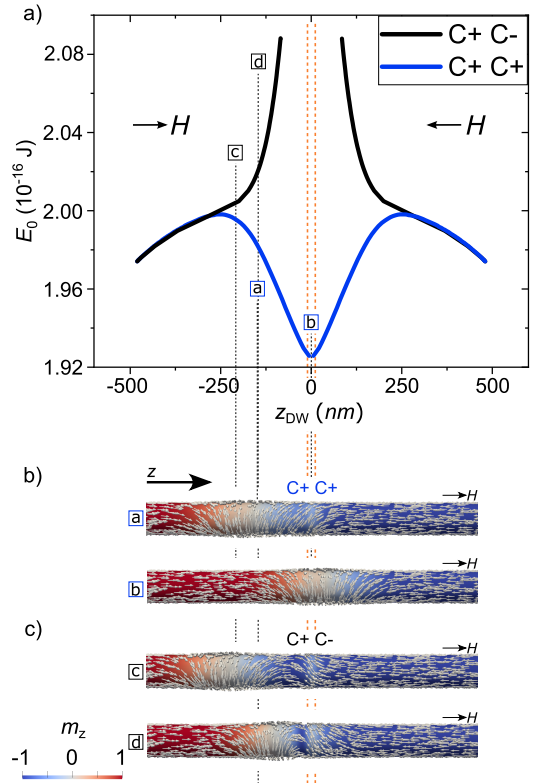


Figure 1. a) Internal energy E_0 versus head-to-head BPW position (z_{DW}) in a 90 nm diameter Permalloy nanowire with a 20 nm-long chemical modulation centered at $z = 0$. Orange dashed lines indicate the two interfaces of the modulation. The wall is driven towards the modulation by an axial quasi-static magnetic field of rising magnitude oriented along \hat{z} or $-\hat{z}$ for $z_{\text{DW}} < 0$ or $z_{\text{DW}} > 0$, respectively. Blue stands for parallel circulations $C + C+$ of the BPW and modulation, while black stands for antiparallel $C + C-$ circulations. b) and c) show outer view configurations obtained with micromagnetic simulations for selected wall positions (z_{DW}) for parallel and antiparallel circulations, respectively. The color code represents m_z .

Experimental evidence of DW pinning and repulsion

We have experimentally probed the effectiveness of chemical modulations as pinning sites for domain walls, previously nucleated by applying a magnetic field of around 1 T perpendicular to the wire axis or by injecting a 10 ns-long

pulse of current with amplitude $1 \times 10^{12} \text{ A} \cdot \text{m}^{-2}$. We image the magnetization states in the wires with either full field or scanning Transmission X-ray microscopy, as well as with X-ray ptychography, all combined with XMCD. The combination of high spatial resolution and direct probing of magnetization enables the extraction of unambiguous information about the DW type and inner structure. Figure 2a

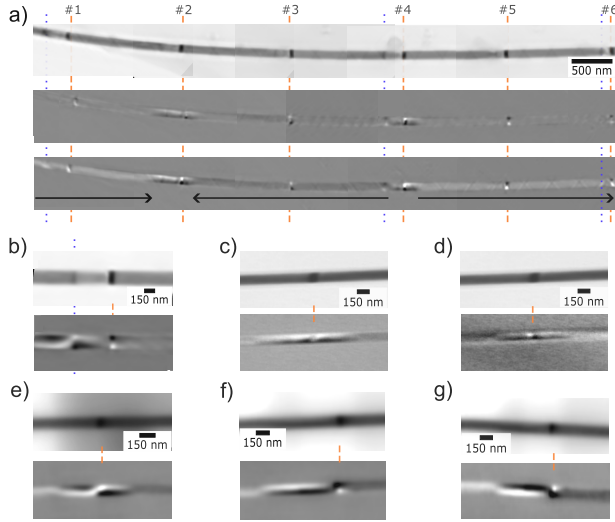


Figure 2. X-ray magnetic imaging of domain walls in different Permalloy nanowires with periodic $\text{Fe}_{80}\text{Ni}_{20}$ chemical modulations. **a), b), e), f), g)** Top: transmission amplitude ptychographic reconstruction image at the Fe L_3 edge. Orange dashed lines indicate the location of the chemical modulations. Blue dotted lines indicate the location of Fe-rich minor modulations. Bottom: corresponding reconstructed amplitude ptychographic XMCD image. **c), d)** Top: TXM image at the Fe L_3 edge and Fe L_2 edge, respectively. Bottom: corresponding XMCD image. Images show BPW pinning at **(a), (c), (d))** or next to **(f), (g))** a chemical modulation, and TVW pinning at **(e))** or next to **(b))** a chemical modulation. System geometry: **a), b):** $d = 130 \text{ nm}$, $l = 60 \text{ nm}$, **c), d):** $d = 105 \text{ nm}$, $l = 100 \text{ nm}$, and **e), f), g):** $d = 120 \text{ nm}$, $l = 30 \text{ nm}$.

shows composite transmission amplitude ptychographic reconstruction and XMCD images at the Fe L_3 edge of a 130 nm-diameter Permalloy nanowire with periodic 60 nm-long $\text{Fe}_{80}\text{Ni}_{20}$ chemical modulations. The darker regions in the transmission image marked with orange dashed lines are the Fe-rich chemical modulations (higher absorption). A closer look reveals a depletion in the Fe content at the left of some of the chemical modulations, extending over a few hundreds of nanometers and ending with a short Fe-rich minor modulation (see blue dotted line, *e.g.*, modulation #4). This material inhomogeneity arises from an instability occurring during the electroplating process. Based on this finding, the synthesis was revisited to avoid this defect. Corresponding images will be shown later on, but magnetic images of this first generation of wires are informative on their own.

The XMCD images in Figure 2a correspond to the wire axis perpendicular to the X-ray beam (middle), and with a 10° offset (bottom). The former is insensitive to the axial magnetization component. Therefore, the neutral gray level in the Permalloy segments reveals that they are uniformly magnetized along the axis. In contrast, a strong dark/bright contrast arises on either side of the wire at every modulation, indicative of magnetization curling around the axis.²¹ Note that for a given magnetization component, we expect XMCD to be stronger for Fe-rich areas due to the stronger absorption,¹³ so that the displayed contrast does not reflect quantitatively the magnetization state. The image with

the tilted sample offers a light dark and bright contrast reflecting axial magnetization in the segments, revealing the occurrence of three domains (black arrows). The stronger magnetic contrast at modulations #2 and #4 can now be understood as the signature of BPWs, while the lighter contrast at the other modulations simply reflects spontaneous curling of magnetization due to the mismatch of magnetization magnitude. The two DWs pinned at modulations #2 and #4 confirm the potential of modulations to pin DWs. A close look shows that the DW is centered exactly on the main modulation, while the secondary chemical modulation also induces a slight curling, which may be either parallel (modulation #2) or antiparallel (modulation #4) to that of the BPW. This complex modulations can give rise to other pinning situations, such as illustrated in Figure 2b. Here, the DW is of TVW type and is pinned at the secondary chemical modulation. This highlights the generality of the pinning potential of modulations, regardless of their strength and the type of DW. One may wonder whether this configuration results from the exchange-driven repulsion between the modulation and the opposite circulation on the right side of the TVW, outlined previously, however, the existence of the secondary modulation biases the discussion.

To get a conclusive view, we now examine the situation of symmetric chemical modulations, *i.e.*, after refining the synthesis process, and with a variety of wire diameters and lengths of chemical modulation (Figure 2c-g). Domain walls of either BPW (Figure 2c-d) or TVW type (Figure 2e) can be pinned exactly at the modulation. Note that Figure 2c and Figure 2d are of the same modulation imaged at the Fe L_3 and Fe L_2 , respectively, in a case where a too high absorption at the L_3 edge resulted in saturation and thus absence of magnetic contrast.¹³ BPWs can also be found very close to a modulation, in situations where the sign of circulation of the DW and modulation are opposite (Figure 2f-g). This is consistent with the micromagnetic simulations which showed that modulations can give rise to a potential well to pin DWs, but in case of opposite circulation situation there exists a strong repulsive potential, so that the DW stops just before the modulation.

Propagation of DWs through modulations

We now consider the magnetization process of domain-wall motion across a modulation under the stimulus of an external axial magnetic field, for both parallel and antiparallel magnetization circulation between BPW and modulation.

The case of identical circulations – Smooth propagation

In this section, we consider the situation where the BPW and the chemical modulation exhibit the same sign of circulation. We start with micromagnetic simulations of a 90 nm diameter Permalloy nanowire, with either a 20 nm or a 100 nm-long chemical modulation. The initial state is a head-to-head BPW located at $z_{\text{DW}} = -500 \text{ nm}$, which we push towards the modulation by applying a positive magnetic field. The strength of the magnetic field is increased in the form of plateaus of length 2 ns and rising magnitude. The damping coefficient is $\alpha = 1$, to mimic a quasistatic situation. We chose a positive circulation in both modulation and BPW,

which is the stable one during motion along $+\hat{z}$ in a homogeneous wire.⁴⁶

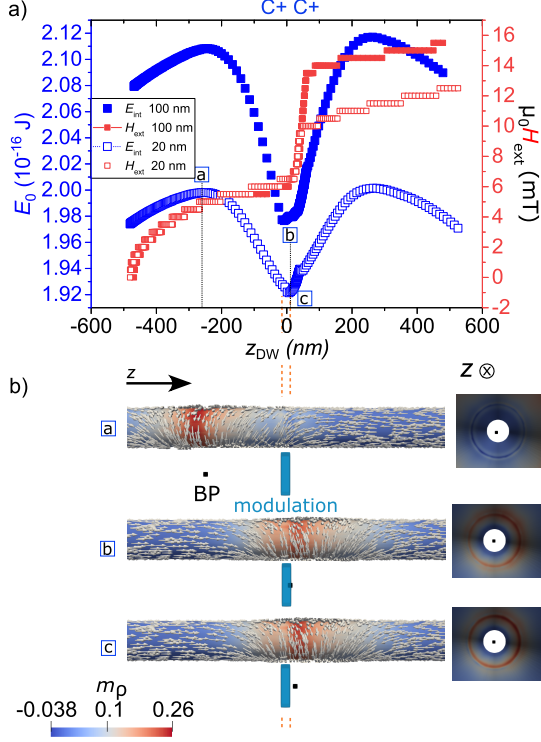


Figure 3. BPW propagation through a chemical modulation in a 90 nm-diameter Permalloy nanowire for parallel and positive circulations $C+C+$ with respect to \hat{z} . **a)** Internal energy E_0 versus BPW position (z_{DW}). Open and full blue symbols correspond to a chemical modulation length of 20 nm and 100 nm, respectively. Red symbols show the magnitude of the axial magnetic field, applied in plateaus of duration 2 ns and rising magnitude. **b)** Outer (left) and inner (right) micromagnetic views at selected z_{DW} , for a modulation length of 20 nm. Each configuration is identified with a letter in **a)**. The black square corresponds to the Bloch point position and the elongated light blue rectangle to the position of the chemical modulation, whose interfaces are indicated by the orange dashed lines. The color code represents m_ρ .

Figure 3a shows the internal energy of the system as a function of z_{DW} . The open blue symbols depict the scenario of a chemical modulation with a length of 20 nm, while the filled blue symbols depict the scenario with a chemical modulation with a length of 100 nm. The red symbols indicate the linearly-increasing strength of the magnetic field, with plateaus of duration 2 ns. The two energy profiles are qualitatively similar, with a well at the modulation and long-distance repulsion, consistent with Figure 1a. Initially, the DW is located on the left-hand side of the modulation in the repulsive area, and the field needs to be increased to about 3 mT to overcome the axial gradient of internal energy (Note that the DW is already continuously drifting during each of the 2 ns-long plateaus at the top of the energy barrier, around $z_{DW} = -200$ nm, so that the value of the magnetic field when at this position is an upper value of the propagation field). Then, the DW remains pinned close to the bottom of the energy well over a wide range of values of applied field, which is illustrated by the sharp slope of the red curves. Finally, the DW depins from the modulation and starts drifting again to the right. The depinning field is ≈ 10 mT and ≈ 14 mT for the short and long modulations, respectively. The propagation and depinning fields more or less reflect the value of steepest slope of internal energy, consistent with the Becker-Kondorsky model.

In the case of the longer modulation the internal energy is shifted upwards even when the DW is away from the modulation, reflecting the higher cost associated with curling in the longer segment.²¹ The upward shift is reduced at rest likely because most of the curling of the BPW fits within the modulation, so that the cost of exchange required anyway by the modulation, benefits the BPW. This results in a deeper energy well for the longer modulation, and thus a larger depinning field. Finally, note that the energy peak for $z_{DW} > 0$ is higher than for $z_{DW} < 0$, contrary to the energy landscape computed in Figure 1a. This is probably related to the slight change of the inner structure of the BPW due to the applied field, which is different when entering versus leaving the modulation.

As the peripheral curling and the Bloch point may follow different dynamics during the motion of a BPW,⁴⁹ it is interesting to track the Bloch point during the propagation/pinning/depinning process, which is illustrated in Figure 3b. On the left, an external view of the magnetization field at the wire surface is shown with gray arrows. The background color codes the radial component of magnetization m_ρ , and thus the location of the wall, as it results from the associated head-to-head charges.⁴⁶ Below each view, the black square indicates the axial position of the Bloch point. On the right side, an internal surface view through the nanowire illustrates the radial position of the Bloch point. The Bloch point deviates only slightly in a minor fashion from the center of mass of the wall. It is ahead of the wall in the repulsive region, and tends to be pinned at interfaces of the modulation. Hence, we conclude that a BPW propagates smoothly through a chemical modulation, when their circulation senses are parallel.

Experimental evidence of BPW depinning, motion and repinning

In the following, we provide experiments supporting the micromagnetic predictions. We consider a 130 nm-diameter Permalloy nanowire with two 60 nm-long chemical modulations separated by a distance of 2 μ m, shown in Figure 4. Note that this is a situation of asymmetric modulations, with a Fe-depleted segment on the left-hand side of the modulation, ending with a narrow Fe-rich secondary modulation. The initial state is a head-to-head DW located at the right modulation, labeled #2. There is no DW at the left modulation, labeled #1, but its circulation is of the same sign. We apply a dc axial magnetic field, that tends to move the DW to that second modulation. Initially, the domain wall center seems to lie between the main and the secondary modulations of #2. At a critical field of 9 mT, the BPW is depinned and moves left, still being connected to the secondary modulation. At 11 mT, the BPW propagates along the entire Permalloy segment until modulation #1. Upon removal of the magnetic field, the BPW relaxes, shifting slightly to the right side. This slight shift may be attributed to the opposing curling circulation in the secondary modulation of #1, inducing a repulsion of the BPW towards the opposite direction. Therefore, we have confirmed experimentally the order of magnitude of the pinning and depinning strength at the modulations for parallel circulations. The data also illustrates controlled pinning, stronger than the intrinsic pinning on material defects along the Permalloy segments.

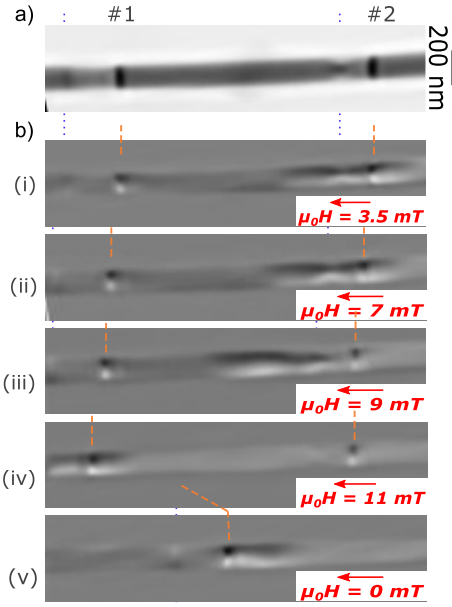


Figure 4. X-ray imaging of BPW depinning, propagation and repinning on chemical modulations under an axial dc magnetic field. The wire of 130 nm diameter is made of Permalloy with periodic 60 nm-long $\text{Fe}_{65}\text{Ni}_{35}$ chemical modulations, indicated with orange vertical dashed lines. Blue dotted lines indicate the location of Fe-rich minor modulations. Imaging is performed at the Fe L_3 edge. **a)** Ptychographic XAS image a BPW pinned at modulation #2. **b)** Corresponding XMCD images taken under a constant magnetic field, indicated in red.

The case of opposite circulations – Modulations as a polarizing component

In addition to the above, we now consider the propagation of a BPW through a chemical modulation, with initially antiparallel circulation. We expect a behavior different from the case of identical circulation, as the modulation should act as an energy barrier to the domain wall (Figure 1). The initial configuration is a head-to-head BPW at $z_{\text{DW}} = -500$ nm and a chemical modulation at $z_{\text{DW}} = 0$. The magnetic field strength is increased linearly, and a damping coefficient $\alpha = 1$ is used, in order to mimic a quasistatic situation. The circulation is initially positive in the BPW, which is the stable one during motion along $+\hat{z}$ in a homogeneous wire.

Figure 5a shows the DW internal energy during its propagation through the modulation, along with selected micromagnetic views and tracking of the Bloch point. The left and right panels correspond to a chemical modulation length of 20 nm and 100 nm, respectively. The energy profiles are similar to those in Figure 1 for $z_{\text{DW}} \lesssim 200$ nm, *i.e.*, an energy barrier due to the magnetostatic-driven repulsion. However, the situation changes drastically at later stages, although reminiscent of a potential well for $z_{\text{DW}} \gtrsim 200$ nm. First, the profiles are largely asymmetric when comparing the left and right sides of the modulation. Second, discontinuities of the internal energy are observed. Third, the propagation field is considerably larger than for identical circulations $C + C+$, *e.g.*, 18 mT for a 20 nm-long modulation. For the case of a 100 nm-long modulation, the depinning field reaches 32 mT. All this hints at a drastically-different propagation mechanism than in the case of $C + C+$, which we examine now in more detail.

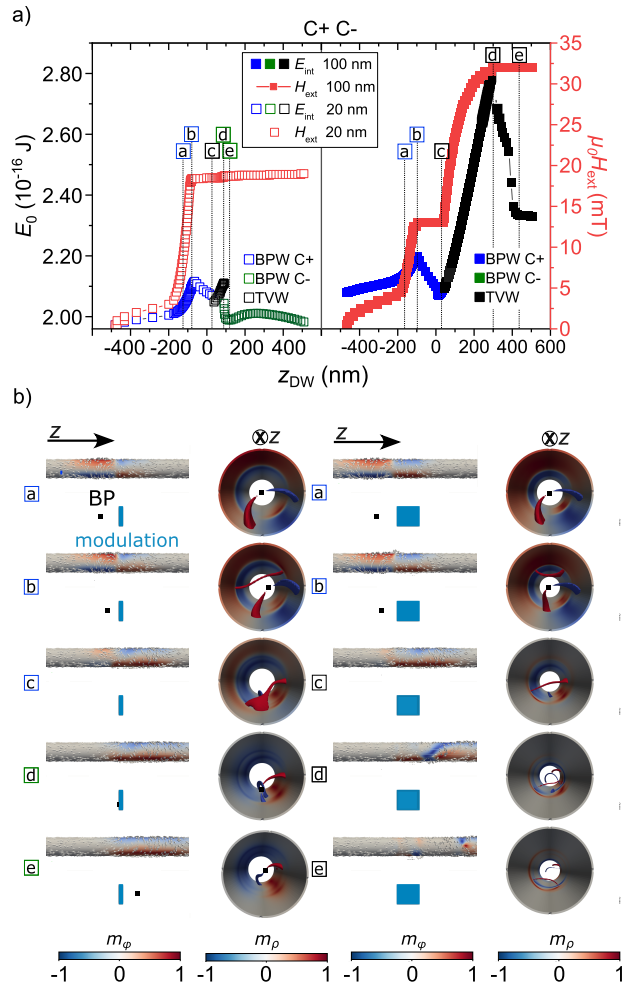


Figure 5. BPW $C+$ propagation through a chemical modulation of opposite circulation $C-$ for a 90 nm-diameter Permalloy nanowire. **a)** Internal energy E_0 versus BPW position z_{DW} . Left and right panels illustrate the case of chemical modulation lengths of 20 nm (open symbols) and 100 nm (filled symbols), respectively. Red symbols denote the amplitude of the axial magnetic field, increased every 2 ns. Blue, black and green symbols represent the internal energy for DW configurations of BPW $C+$, TVW and BPW $C-$, respectively. **b)** Simulated micromagnetic states shown from outer and inner perspectives at selected z_{DW} indicated by black dashed lines in **a)**. The color code denotes m_ϕ and m_ρ , respectively. The black square corresponds to the Bloch point position, while the elongated blue rectangle indicates the chemical modulation.

Figure 5b displays the micromagnetic simulations outer views and surface inner views. The color code denotes the azimuthal m_ϕ and radial magnetization m_ρ , respectively. The black square indicates the Bloch point position, while the elongated blue rectangle denotes the chemical modulation. Labels on the left correspond to configurations at various z_{DW} values indicated by the black dashed lines in Figure 5a. Upon analyzing the temporal evolution of these configurations, several key observations emerge: initially, the BPW and modulation display opposite m_ϕ contrast due to their antiparallel circulations (labeled as *a*). At this point the inner view presents $m_\rho = \pm 1$ isolines in the bulk connecting the surface to the Bloch point. As the BPW approaches the modulation it shrinks while increasing in energy (blue symbols in Figure 5a). At the point labeled as *b*, a new isoline $m_\rho = 1$ crosses the bulk, ending by the disappearance of the blue isoline $m_\rho = -1$ with the Bloch point, resulting in a TVW-type DW (labeled as *c*). Note that between *b* and

c the topology of the wall remains that of a BPW.^{29,50} The TVW-type configuration is represented by the black symbols in Figure 5a. Following this, the evolution diverges for short and large modulation lengths. For short modulations of 20 nm length (left panel), the energy increases reaching a maximum of 2.11×10^{-16} J, at which point the Bloch point reappears in the volume and pins onto the chemical modulation (labeled as *d*). At this stage, the Bloch point lags behind the BPW (see state *d* in the outer-micromagnetic view), indicating a state far from equilibrium. The equal m_ϕ contrast in wall and modulation illustrates a reversal of BPW circulation. The BPW configuration with negative circulation is represented by the green symbols in Figure 5a, which indicate the subsequent decrease in energy associated with depinning (labeled as *e*), followed by a potential well for parallel circulations, as illustrated in Figure 1. In contrast, for a 100 nm modulation, the energy increases further, up to 2.79×10^{-16} J, until the TVW-type configuration propagates through the modulation (labeled as *d*). This is followed by a decrease in energy until the TVW depins from the modulation and propagates freely along \hat{z} (labeled as *e*). Subsequently, the Bloch point re-enters the volume, and a BPW *C-* of reversed circulation keeps propagating (not shown). The larger deppening field induces a high excitation to the system causing the re-injection of the Bloch point in the volume (or transformation to BPW *C-*) at $z_{\text{BPW}} > 600$ nm.

To better understand the microscopic mechanism of the domain wall transformation, and link it to the non-trivial energy evolution in Figure 5, it is helpful to perform a topological analysis.⁵⁰ To mimic a more realistic situation, the simulations were conducted with an $\alpha = 0.02$ and an axial magnetic field of 50 mT. The tracking of the volume and surface singularities was performed by using a post-processing tool. Figure 6a displays the outer micromagnetic view of the initial state. The color code corresponds to the azimuthal magnetization, being red for the BPW curling along $+m_\phi$ and blue for the chemical modulation magnetized along $-m_\phi$. The three-dimensional view in Figure 6b displays the trace of the Bloch point (in black) and surface vortex-antivortex pairs (in colors). The chemical modulation is represented by the grey disk. The displacement of the Bloch point occurs along the wire axis as is well known for domain wall motion in an homogeneous nanowire.⁵¹ Upon approaching the chemical modulation, the Bloch point travels towards the surface until it annihilates with a surface vortex or antivortex (labeled *out*). Subsequently, an azimuthal displacement of the latter occurs until a Bloch point is injected into the volume (labeled *in*) and propagates through the chemical modulation.

The evolution of the two vortex-antivortex pairs is displayed in Figure 6d along the axial \hat{z} and azimuthal $\hat{\phi}$ directions. It is important to note that here we depict a zoom of the critical events, while the Bloch point (represented by the black symbols) has existed in the system since $t = 0$. The first pair nucleated $V_1^+ - AV_1^+$ shows positive polarity (red and orange lines), whereas the second pair $V_2^- - AV_2^-$ shows negative polarity (blue and green lines). Within each V-AV pair, the vortex and antivortex move away from each other along the azimuthal direction. We believe that the polarity of the first pair appearing can be understood as it matches the polarity of the head-to-head BPW, and also the one favored by the chirality of the Landau-Lifshitz-Gilbert (LLG) equation via $\mathbf{H} \times \mathbf{M}$. The reason for the opposite polarity of the second pair is probably to reduce the global

magnetostatic energy. Overall, the detailed process involves the Bloch point reaching the surface at the moment when the vortex with negative polarity V_2^- (blue) and the antivortex with positive polarity AV_1^+ (orange) merge. At this precise moment, only V_1^+ and AV_2^- remain in the system far from each other. Later, a Bloch Point with negative polarity re-enters in the volume as V_1^+ and AV_2^- annihilate.

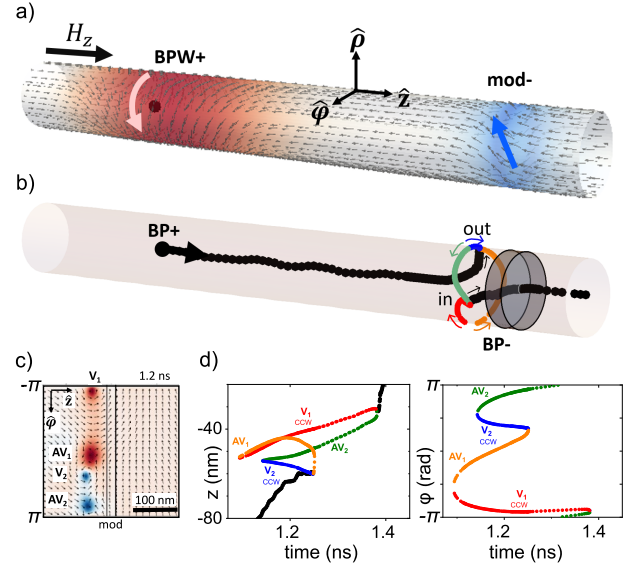


Figure 6. Topology of field-driven BPW circulation switching prior to propagate through a chemical modulation of antiparallel circulation. **a)** Outer micromagnetic view of the initial state, with a BPW of positive circulation and a modulation of negative circulation with respect to \hat{z} . The color code represents m_ϕ . **(b)** Black: Bloch point trajectory while crossing the modulation under an axial field of 50 mT. Color: generated pairs of vortex and antivortex on the surface. **(c)** Unrolled surface of the wire showing the vortex/antivortex pair formation to the left of the modulation. The color code represents m_ϕ . **(d)** Temporal evolution along \hat{z} and $\hat{\phi}$ of Bloch point (black) and vortex-antivortex pairs (colored curves).

The phenomenon of BPW circulation switching upon crossing a chemical modulation under a magnetic field represents a novel discovery. Nevertheless, the underlying mechanism mirrors the one reported in ref Riz et al.²⁹ for BPW switching in an homogeneous nanowire driven by an antiparallel Oersted field, sharing the same topological features. We can draw an analogy between this phenomenon and the mechanisms of coherent reversal versus nucleation-propagation for the magnetization reversal of magnetic systems: the switching of BPW circulation via the homogeneous rise of m_ϕ to ± 1 on the wire periphery would imply a substantial dipolar energy cost. Instead, here we observe the local nucleation of an area with $m_\phi = \pm 1$, which then propagates around the perimeter through the motion of surface vortex-antivortex pairs along opposite azimuthal directions.

Regarding the switching of BPW in a homogeneous or in chemically-modulated system, it is important to note the distinctions between the two scenarios. The unrolled map of Figure 6c illustrates that the vortex-antivortex pairs nucleate always on the same side of the BPW, between the BPW interface and the chemical modulation. This contrasts with the scenario of the Oersted field induced BPW switching on a homogeneous nanowire (without chemical modulation), where one vortex or antivortex of same polarity appears at each side of the wall.²⁹ Here, the strong exchange interaction with the opposite circulation of the modulation acts in

a very similar fashion to an Ersted field, but on one side only of the DW.

Conclusion

In summary, we have experimentally outlined and analyzed, through micromagnetic simulations, the interaction between higher-magnetization chemical modulations and Bloch Point walls (BPWs) in cylindrical nanowires. These modulations act as local potential wells, that effectively pin domain walls due to their shared azimuthal curling, thereby lowering the total energy of the system. However, the mechanism of propagation through a modulation is complex. At distances larger than the BPW width, the interaction is primarily repulsive, driven by magnetostatics. As the distance decreases, exchange interactions become significant, breaking the degeneracy between cases of identical or opposite circulation senses in the wall and the modulation. In the former case, the BPW can propagate through the modulation relatively unchanged, although the depinning field is higher than the field required to push the wall into the energy well of the modulation. For opposite circulations, the modulation forces the BPW to change its circulation before propagation can occur, effectively acting as a polarizing device. This process involves the annihilation/re-nucleation of a Bloch point and a transient topology state of a transverse-vortex wall, a phenomenon reported here for the first time. This process is similar, and thus consistent, with the change of domain wall type in homogeneous nanowires driven by field or Ersted-field, shedding light on the generality of the phenomenon. These findings open the possibility of utilizing chemical modulations as a polarizing component, thereby allowing the control of the internal structure of domain walls.

Methods

Permalloy ($\text{Fe}_{20}\text{Ni}_{80}$) cylindrical nanowires with Fe-rich chemical modulations were synthesized by single-bath template-assisted electrochemical deposition. Nanoporous anodic aluminum oxide (AAO) templates were prepared by hard anodization of Al disks (Goodfellow, 99.999% in purity) in a water-based solution of oxalic acid (0.3 M) and ethanol (0.9 M), applying 140 V of anodization voltage at 0 °C to 1 °C for 2.5 h. The remaining Al was etched with an aqueous solution of CuCl_2 (0.74 M) and HCl (3.25 M), the oxide barrier was removed and the pores opened to a final diameter of ≈ 120 nm with H_3PO_4 (5 % vol.).

The growth conditions were similar to those described in ref Ruiz-Gómez et al.⁵². For chemical modulations with a length below 60 nm, the composition was $\text{Fe}_{65}\text{Ni}_{35}$, while for lengths above 60 nm, the composition was $\text{Fe}_{80}\text{Ni}_{20}$. After the electrochemical growth, the AAO templates were dissolved in H_3PO_4 (0.4 M) and H_2CrO_4 (0.2 M). Then, the nanowires were dispersed on 20 nm thick Si_3N_4 windows to allow for transmission microscopy. To nucleate domain walls, nanowires were contacted electrically using laser lithography in order to allow the injection of GHz bandwidth electric pulses. Resistivity values obtained are around $20 \mu\Omega \cdot \text{cm}$. To prevent sample oxidation and to increase thermal transfer to the Si_3N_4 , a 20 nm-thick layer of Al_2O_3 was deposited on the device by Atomic Layer Deposition (ALD). Additionally, 100 nm of Al was deposited on the backside of the substrate.

The wires were imaged with X-ray Magnetic Circular Dichroism (XMCD) coupled to Transmission X-ray Microscopy (TXM)⁵³ at the MISTRAL beamline of ALBA Synchrotron and by X-ray ptychography^{54–56} at HERMES STXM beamline of SOLEIL synchrotron. The photon energy was set to the Fe L_3 absorption edge, and the sample holder could be rotated from the plane normal to the X-ray incidence in order to be sensitive to both axial and azimuthal magnetization components. During TXM imaging, series of about 64 images per polarity were acquired, registered and averaged in order to increase the signal-to-noise ratio, while keeping under control the loss of spatial resolution due to time drift. Ptychographic reconstruction was carried out using the open-source PyNX software developed at the European Synchrotron Radiation Facility.⁵⁷ If not initially present, DWs were nucleated in situ by applying a 10 ns-long pulse of current with amplitude $1 \times 10^{12} \text{ A} \cdot \text{m}^{-2}$. We performed micromagnetic simulations with the *mumax3* code.⁵⁸ The system considered is a cylindrical Permalloy nanowire of 90 nm diameter and 2 μm length, with a 20 nm-long or 100 nm-long $\text{Fe}_{80}\text{Ni}_{20}$ chemical modulation at its center. In order to mimic an infinite wire, the magnetic charges at the wire ends were removed numerically. The mesh size used was 2 nm. The following material parameters were used:⁵⁹ spontaneous magnetization $M_1 = 8 \times 10^5 \text{ A/m}$ for the Permalloy segments, $M_2 = 14 \times 10^5 \text{ A/m}$ for the chemical modulation, single exchange stiffness for all materials $A = 1.3 \times 10^{-11} \text{ J/m}$ and zero magnetocrystalline anisotropy. The choice of an identical value for exchange stiffness stems from the similarity of ordering temperature for the two compositions. The resulting dipolar exchange lengths are 5.6 nm and 3.3 nm, respectively. To study static or quasi-static dynamics a damping term of $\alpha = 1$ was used. The initial state considered was a BPW at $z = \pm 500$ nm and a chemical modulation centered at $z = 0$. Circulations of both the BPW and the modulation are defined arbitrarily with respect to $+\hat{z}$, and labeled $C+$ for positive and $C-$ for negative.

When the tracking of topological elements characterizing the type of wall is required (Bloch point for BPW, surface vortex/antivortex for the TVW), we use an in-house post-processing tool, developed specifically for tetrahedron-based finite-elements.⁵⁰ Therefore, in this case the micromagnetic simulations were conducted with *feeLLGood* code,^{60–63} a home-made micromagnetic code based on finite-element methods.

Acknowledgement This work received financial support from the French RENATECH network, implemented at the Upstream Technological Platform in Grenoble PTA (ANR-22-PEEL-0015), and from the French National Research Agency (Grant No. ANR-17-CE24-0017 MATEMAC-3D; Grant ANR-22-CE24-0023 DIWINA), from the Spanish (MCIN/AEI/10.13039/501100011033 through Projects PID2020-117024GB-C43, TED2021-130957B-C52 and CEX2020- 001039-S). S. R-G acknowledges support from the Humboldt foundation grant 1223621 and Marie Curie fellowship grant GAP-101061612. M. F. acknowledges the funding from MICIN through grant number PID2021-122980OB-C54. We acknowledge support from the team of the Nanofab platform (CNRS Néel institut), from the ALBA in-house research program and MISTRAL and CIRCE beamlines and from the SOLEIL HERMES beamline.

References

- (1) Arrott, A. S.; Heinrich, B.; Aharoni, A. Point singularities and magnetization reversal in ideally soft ferromagnetic cylinders. *IEEE Trans. Magn.* **1979**, *15*, 1228.
- (2) Hinzke, D.; Nowak, U. Magnetization switching in nanowires: Monte Carlo study with fast Fourier transformation for dipolar fi. *J. Magn. Magn. Mater.* **2000**, *221*, 365.
- (3) Zeng, H.; Skomski, R.; Menon, L.; Liu, Y.; Bandyopadhyay, S.; Sellmyer, D. J. Structure and magnetic properties of ferromagnetic nanowires in self-assembled arrays. *Phys. Rev. B* **2002**, *65*, 134426.
- (4) Hertel, R. Computational micromagnetism of magnetization processes in nickel nanowires. *J. Magn. Magn. Mater.* **2002**, *249*, 251.
- (5) Bran, C.; Fernandez-Roldan, J. A.; Palmero, E. M.; Berganza, E.; Guzman, J.; del Real, R. P.; Asenjo, A.; Rodriguez, A. F.; Foerster, M.; Aballe, L.; Chubykalo-Fesenko, O.; Vazquez, M. Direct Observation of Transverse and Vortex Metastable Magnetic Domains observed in Cylindrical Nanowires. *Phys. Rev. B* **2017**, *96*, 125415.
- (6) Vila, L.; Darques, M.; Encinas, A.; Ebels, U.; George, J.-M.; Faini, G.; Thiaville, A.; Piroux, L. Magnetic vortices in nanowires with transverse easy axis. *Phys. Rev. B* **2009**, *79*, 172410.
- (7) Ivanov, Y. P.; Vivas, L. G.; Asenjo, A.; Chuvilin, A.; Chubykalo-fesenko, O.; Vazquez, M. Magnetic structure of a single-crystal hcp electrodeposited cobalt nanowire. *Europhys. Lett.* **2013**, *102*, 17009.
- (8) Chen, F.; Wang, F.; Jia, F.; Li, J.; Liu, K.; Huang, S.; Luan, Z.; Wu, D.; Chen, Y.; Zhu, J.; Peng, R.-W.; Wang, M. Periodic magnetic domains in single-crystalline cobalt filament arrays. *Phys. Rev. B* **2016**, *93*, 054405.
- (9) Kan, J. J.; Lubarda, M. V.; Chan, K. T.; Uhlir, V.; Scholl, A.; Lomakin, V.; Fullerton, E. E. Periodic chiral magnetic domains in single-crystal nickel nanowires. *Phys. Rev. Mater.* **2018**, *2*.
- (10) Chien, C. L.; Sun, L.; Tanase, M.; Bauer, L. A.; Hultgren, A.; Silevitch, D. M.; Meyer, G.; Searson, P.; Reich, D. H. Electrodeposited magnetic nanowires: arrays, field-induced assembly, and surface functionalization. *J. Magn. Magn. Mater.* **2002**, *249*, 146.
- (11) Wang, T.; Wang, Y.; Fu, Y.; Hasegawa, T.; Oshima, H.; Itoh, K.; Nishio, K.; Masuda, H.; Li, F. S.; Saito, H.; Ishio, S. Magnetic behavior in an ordered Co nanorod array. *Nanotechnology* **2008**, *19*, 455703.
- (12) Vock, S.; Hengst, C.; Wolf, M.; Tschulik, K.; Uhlemann, M.; Sasvari, Z.; Makarov, D.; Schmidt, O. G.; Schultz, L.; Neu, V. Magnetic vortex observation in FeCo nanowires by quantitative magnetic force microscopy. *Appl. Phys. Lett.* **2014**, *105*, 172409.
- (13) Jamet, S.; Col, S. D.; Rougemaille, N.; Wartelle, A.; Locatelli, A.; Mentès, T. O.; Burgos, B. S.; R.Afid; Cagnon, L.; Bachmann, J.; Bochmann, S.; Fruchart, O.; Toussaint, J. C. Quantitative analysis of shadow X-ray Magnetic Circular Dichroism Photo-Emission Electron Microscopy. *Phys. Rev. B* **2015**, *92*, 144428.
- (14) Iglesias-Freire, O.; Bran, C.; Berganza, E.; Mínguez-Bacho, I.; Magén, C.; Vázquez, M.; Asenjo, A. Spin configuration in isolated FeCoCu nanowires modulated in diameter. *Nanotechnology* **2015**, *26*, 395702.
- (15) Bran, C.; Berganza, E.; Palmero, E. M.; Fernandez-Roldan, J. A.; Del Real, R. P.; Aballe, L.; Foerster, M.; Asenjo, A.; Rodríguez, A. F.; Vazquez, M. Spin configuration of cylindrical bamboo-like magnetic nanowires. *J. Mater. Chem. C* **2016**, *4*, 978–984.
- (16) Chandra Sekhar, M.; Liew, H. F.; Purnama, I.; Lew, W. S.; Tran, M.; Han, G. C. Helical domain walls in constricted cylindrical NiFe nanowires. *Appl. Phys. Lett.* **2012**, *101*, 152406.
- (17) Salem, M. S.; Sergelius, P.; Corona, R. M.; Escrig, J.; Görlitz, D.; Nielsch, K. Magnetic properties of cylindrical diameter modulated Ni80Fe20 nanowires: interaction and coercive fields. *Nanoscale* **2013**.
- (18) Nasirpour, F.; Peighambari-Sattari, S.-M.; Palmero, C. B. E. M.; Eguarte, E. B.; Vazquez, M.; Patsopoulos, A.; Kechrakos, D. Geometrically designed domain wall trap in segmented nickel magnetic nanowires for spintronics devices. *Sci. Rep.* **2019**, *9*, 1–11.
- (19) Allende, S.; Altbir, D.; Nielsch, K. Magnetic cylindrical nanowires with single modulated diameter. *Phys. Rev. B* **2009**, *80*, 174402.
- (20) Ruiz-Gómez, S.; Fernández-González, C.; Martínez, E.; Raposo, V.; Sorrentino, A.; Foerster, M.; Aballe, L.; Mascaraque, A.; Ferrer, S.; Pérez, L. Helical surface magnetization in nanowires: the role of chirality. *Nanoscale* **2020**, *12*, 17880–17885.
- (21) Alvaro-Gómez, L. et al. Micromagnetics of magnetic chemical modulations in soft-magnetic cylindrical nanowires. *Phys. Rev. B* **2022**, *106*, 054433.
- (22) Ivanov, Y. P.; Chuvilin, A.; Lopatin, S.; Kosel, J. Modulated Magnetic Nanowires for Controlling Domain Wall Motion: Toward 3D Magnetic Memories. *Am. Chem. Soc. Nano* **2016**, *10*, 5326.
- (23) Berganza, E.; Jaafar, M.; Bran, C.; Fernández-Roldán, J. A.; Chubykalo-Fesenko, O.; Vázquez, M.; Asenjo, A. Multisegmented Nanowires: a Step towards the Control of the Domain Wall Configuration. *Sci. Rep.* **2017**, *7*, 11576.
- (24) Andersen, I. M.; Wolf, D.; Rodríguez, L. A.; Lubk, A.; Oliveros, D.; Bran, C.; Niermann, T.; Rößler, U. K.; Vazquez, M.; Gatel, C.; Snoeck, E. Field tunable three-dimensional magnetic nanotextures in cobalt-nickel nanowires. *Phys. Rev. Research* **2021**, *3*, 033085.
- (25) Reyes, D.; Biziere, N.; Warot-Fonrose, B.; Wade, T.; Gatel, C. Magnetic Configurations in Co/Cu Multilayered Nanowires: Evidence of Structural and Magnetic Interplay. *Nano Lett.* **2016**, *16*, 1230–1236.
- (26) Franchin, M.; Knittel, A.; Albert, M.; Chernyshenko, D. S.; Fischbacher, T.; Prabhakar, A.; Fangohr, H. Enhanced spin transfer torque effect for transverse domain walls in cylindrical nanowires. *Phys. Rev. B* **2011**, *84*, 094409.
- (27) Schöbitz, M. et al. Fast domain walls governed by topology and Cested fields in cylindrical magnetic nanowires. *Phys. Rev. Lett.* **2019**, *123*, 217201.
- (28) Fernandez-Roldan, J. A.; del Real, R. P.; Bran, C.; Vazquez, M.; Chubykalo-Fesenko, O. Electric current and field control of vortex structures in cylindrical magnetic nanowires. *Phys. Rev. B* **2020**, *102*, 024421.
- (29) Riz, A. D.; Hurst, J.; Schöbitz, M.; Thirion, C.; Bachmann, J.; Toussaint, J. C.; Fruchart, O.; Gusakova, D. Mechanism of fast domain wall motion via current-assisted Bloch-point domain wall stabilization. *Phys. Rev. B* **2021**, *103*, 054430.
- (30) Fernandez-Roldan, J. A.; Chubykalo-Fesenko, O. Dynamics of chiral domain walls under applied current in cylindrical magnetic nanowires. *APL Materials* **2022**, *10*, 111101.
- (31) Moreno, J. A.; Kosel, J. Current-induced zero-field domain wall depinning in cylindrical nanowires. *Sci. Rep.* **2022**, *12*.
- (32) Bran, C.; Fernandez-Roldan, J. A.; Moreno, J. A.; Fraile Rodríguez, A.; del Real, R. P.; Asenjo, A.; Saugar, E.; Marqués-Marchán, J.; Mohammed, H.; Foerster, M.; Aballe, L.; Kosel, J.; Vazquez, M.; Chubykalo-Fesenko, O. Domain wall propagation and pinning induced by current pulses in cylindrical modulated nanowires. *Nanoscale* **2023**, *15*, 8387–8394.
- (33) Otalora, J. A.; Cortés-Ortuno, D.; Görlitz, D.; Nielsch, K.; Landeros, P. Oersted field assisted magnetization reversal in cylindrical core-shell nanostructures. *J. Appl. Phys.* **2015**, *117*, 173914.
- (34) Forster, H.; Schrefl, T.; Scholz, W.; Suess, D.; Tsiantos, V.; Fidler, J. Micromagnetic simulation of domain wall motion in magnetic nano-wires. *J. Magn. Magn. Mater.* **2002**, *249*, 181.
- (35) Jamet, S.; Rougemaille, N.; Toussaint, J. C.; Fruchart, O. In *Magnetic Nano- and Microwires: Design, synthesis, properties and applications*; Vazquez, M., Ed.; Woodhead, 2015; Chapter Head-to-head domain walls in one-dimensional nanostructures: an extended phase diagram ranging from strips to cylindrical wires, pp 783–811.
- (36) Döring, W. Point singularities in micromagnetism. *J. Appl. Phys.* **1968**, *39*, 1006.
- (37) Feldtkeller, R. Mikromagnetisch stetige und unstetige Magnetisierungsverteilungen. *Z. Angew. Physik* **1965**, *19*, 530.
- (38) Malozemoff, A. P.; Slonczewski, J. C. *Magnetic domain walls in bubble materials*; Academic press, 1979.
- (39) Da Col, S.; Jamet, S.; Rougemaille, N.; Locatelli, A.; Mentès, T. O.; Burgos, B. S.; Afid, R.; Darques, M.; Cagnon, L.; Toussaint, J. C.; Fruchart, O. Observation of Bloch-point domain walls in cylindrical magnetic nanowires. *Phys. Rev. B* **2014**, *89*, 180405.
- (40) Wartelle, A.; Trapp, B.; Staño, M.; Thirion, C.; Bochmann, S.; Bachmann, J.; Foerster, M.; Aballe, L.; Mentès, T. O.; Locatelli, A.; Sala, A.; Cagnon, L.; Toussaint, J.; Fruchart, O. Bloch-point-mediated topological transformations of magnetic domain walls in cylindrical nanowires. *Phys. Rev. B* **2019**, *99*, 024433, arXiv:1806.10918.
- (41) Kondorski, E. On the nature of coercive force and irreversible changes in magnetisation. *Phys. Z. Sowjetunion* **1937**, *11*, 597.
- (42) Henry, Y.; Ounadjela, K.; Piroux, L.; Dubois, S.; George, J.-M.; Duvail, J.-L. Magnetic anisotropy and domain patterns in electrodeposited cobalt nanowires. *Eur. Phys. J. B* **2001**, *20*, 35.
- (43) Da Col, S.; Jamet, S.; Staño, M.; Trapp, B.; Denmat, S. L.; Cagnon, L.; Toussaint, J. C.; Fruchart, O. Nucleation, imaging, and motion of magnetic domain walls in cylindrical nanowires. *Appl. Phys. Lett.* **2016**, *109*, 062406.
- (44) Schöbitz, M.; Novotný, O.; Trapp, B.; Bochmann, S.; Cagnon, L.; Thirion, C.; Massebœuf, A.; Mossang, E.; Fruchart, O.; Bachmann, J. A Material View on Extrinsic Magnetic Domain Wall Pinning in Cylindrical CoNi Nanowires. *J. Phys. Chem. C* **2023**, *127*, 2387–2397.
- (45) Riz, A. D.; Trapp, B.; Fernandez-Roldan, J.; Thirion, C.; Toussaint, J.-C.; Fruchart, O.; Gusakova, D. *Magnetic Nano- and Microwires*; Elsevier, 2020; pp 427–453.
- (46) Thiaville, A.; Nakatani, Y. In *Spin dynamics in confined magnetic structures III*; Hillebrands, B., Thiaville, A., Eds.; Topics Appl. Physics; Springer: Berlin, 2006; Vol. 101; Chapter Domain-wall dynamics in nanowires and nanostrips, pp 161–205.
- (47) Andreas, C.; Kákay, A.; Hertel, R. Multiscale and multimodel simulation of Bloch-point dynamics. *Phys. Rev. B* **2014**, *89*,

- (48) Wyss, M.; Mehlin, A.; Gross, B.; Buchter, A.; Farhan, A.; Buzzi, M.; Kleibert, A.; Tütüncüoğlu, G.; Heimbach, F.; Fontcuberta i Morral, A.; Grundler, D.; Poggio, M. Imaging magnetic vortex configurations in ferromagnetic nanotubes. *Phys. Rev. B* **2017**, *96*, 024423.
- (49) Hertel, R.; Kirschner, J. Magnetic drops in a soft-magnetic cylinder. *J. Magn. Magn. Mater.* **2004**, *278*, L291.
- (50) Álvaro Gómez, L.; Hurst, J.; Hegde, S.; Ruiz-Gómez, S.; Pereiro, E.; Aballe, L.; Toussaint, J. C.; Pérez, L.; Masseboeuf, A.; Thirion, C.; Fruchart, O.; Gusakova, D. Topological analysis and experimental control of transformations of domain walls in magnetic cylindrical nanowires. 2024.
- (51) Hertel, R. Ultrafast domain wall dynamics in magnetic nanotubes and nanowires. *J. Phys.: Condens. Matter* **2016**, *28*, 483002.
- (52) Ruiz-Gómez, S.; Foerster, M.; Aballe, L.; Proenca, M. P.; Lucas, I.; Prieto, J. L.; Mascaraque, A.; de la Figuera, J.; Quesada, A.; Pérez, L. Observation of a topologically protected state in a magnetic domain wall stabilized by a ferromagnetic chemical barrier. *Sci. Rep.* **2018**, *8*, 16695.
- (53) Sorrentino, A.; Nicolás, J.; Valcárcel, R.; Chichón, F. J.; Rosanes, M.; Avila, J.; Tkachuk, A.; Irwin, J.; Ferrer, S.; Pereiro, E. MISTRAL: a transmission soft X-ray microscopy beamline for cryo nano-tomography of biological samples and magnetic domains imaging. *J. Synchro. Radiat.* **2015**, *22*, 1112–1117.
- (54) Pfeiffer, F. X-ray ptychography. *Nat. Photonics* **2017**, *12*, 9–17.
- (55) Donnelly, C.; Scagnoli, V.; Guizar-Sicairos, M.; Holler, M.; Wilhelm, F.; Guillou, F.; Rogalev, A.; Detlefs, C.; Menzel, A.; Raabe, J.; Heyderman, L. J. High-resolution hard x-ray magnetic imaging with dichroic ptychography. *Phys. Rev. B* **2016**, *94*, 064421.
- (56) Mille, N.; Yuan, H.; Vijayakumar, J.; Stanescu, S.; Swaraj, S.; Desjardins, K.; Favre-Nicolin, V.; Belkhou, R.; Hitchcock, A. P. Ptychography at the carbon K-edge. *Communications Materials* **2022**, *3*.
- (57) Favre-Nicolin, V.; Girard, G.; Leake, S.; Carnis, J.; Chushkin, Y.; Kieffer, J.; Paleo, P.; Richard, M.-I. PyNX: high-performance computing toolkit for coherent X-ray imaging based on operators. *J. Appl. Cryst.* **2020**, *53*, 1404–1413.
- (58) Vansteenkiste, A.; Leliaert, J.; Dvornik, M.; Helsen, M.; Garcia-Sanchez, F.; Waeyenberge, B. V. The design and verification of MuMax3. *AIP Advances* **2014**, *4*, 107133.
- (59) Couderchon, G.; Porteseil, J. L. In *The Iron-Nickel Alloys*; Béranger, G., Duffaut, F., Morlet, J., Thiers, J. F., Eds.; Lavoisier, 1996; Chapter Some properties of nickel-rich commercial Fe-Ni alloys, p 27.
- (60) Alouges, F.; Jaisson, P. Convergence of a finite element discretization for the Landau-Lifshitz equations in micromagnetism. *Math. Models Methods Appl. Sci.* **2006**, *16*, 299–316.
- (61) Alouges, F.; Kritsikis, E.; Toussaint, J.-C. A convergent finite element approximation for Landau-Lifschitz-Gilbert equation. *Physica B* **2012**, *407*, 1345.
- (62) Kritsikis, E.; Vaysset, A.; Buda-Prejbeanu, L.; Alouges, F.; Toussaint, J.-C. Beyond first order finite element schemes for micromagnetics. *J. Comput. Phys.* **2014**, *256*, 357.
- (63) <http://feellgood.neel.cnrs.fr>.